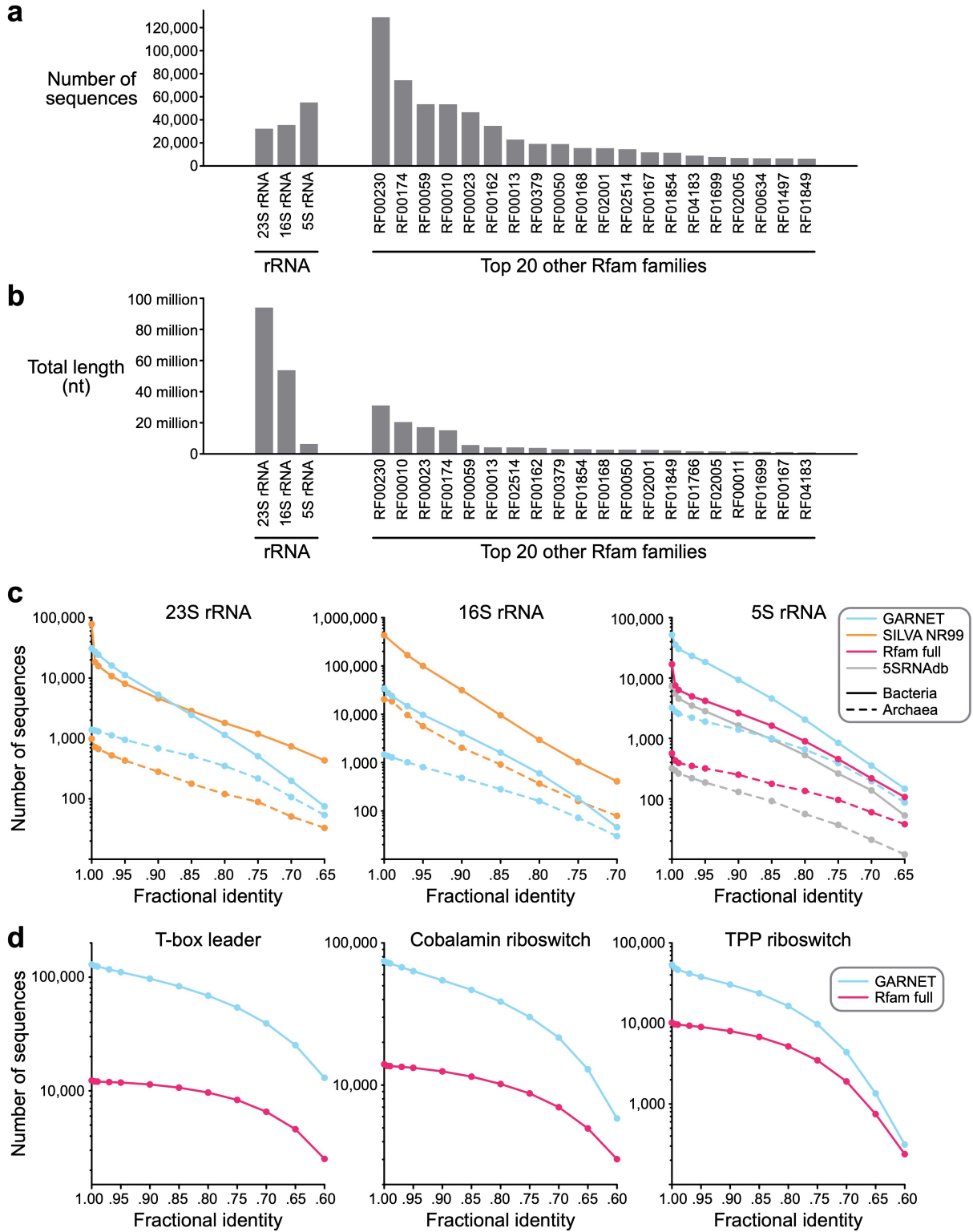
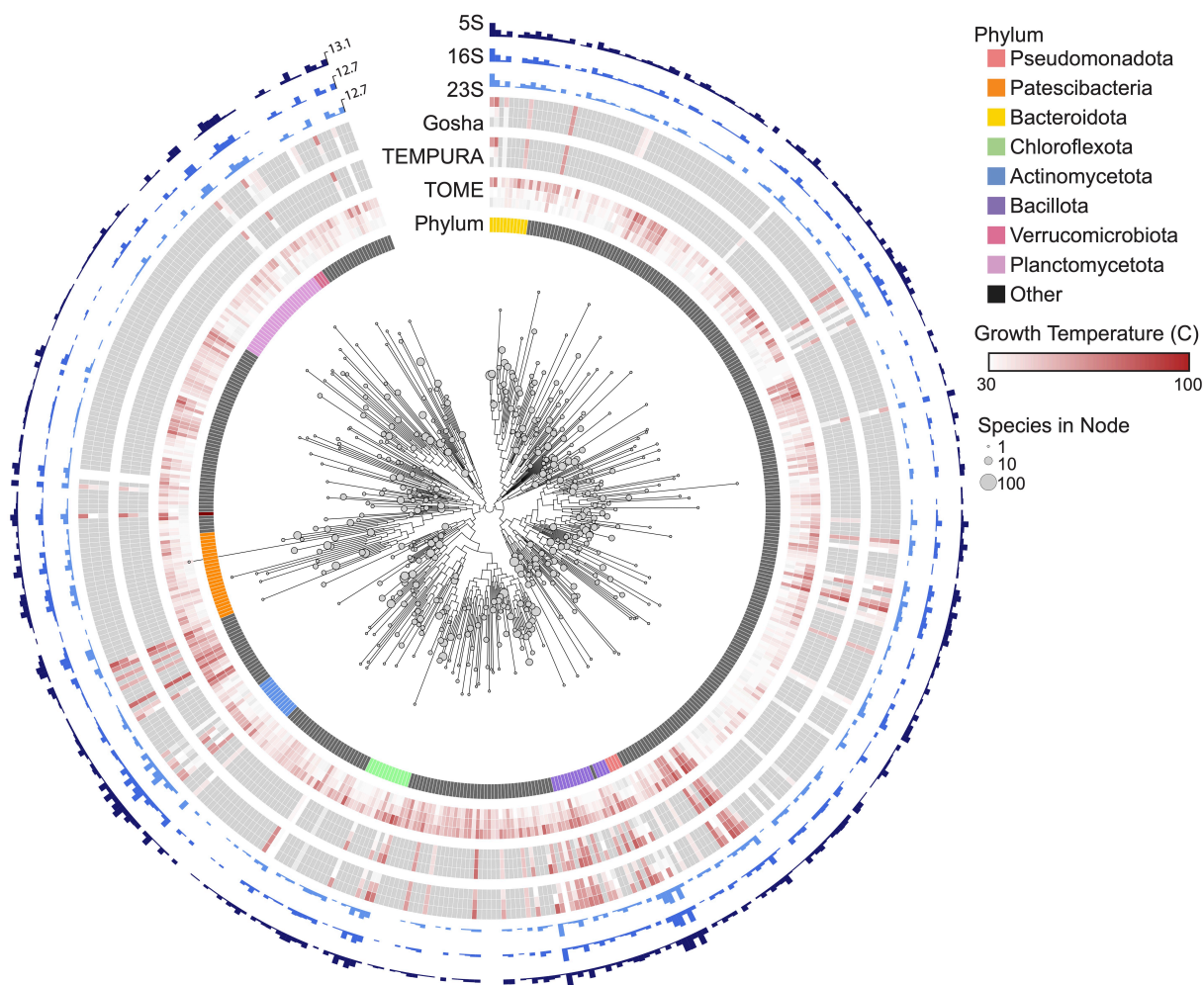


Supplementary Figures

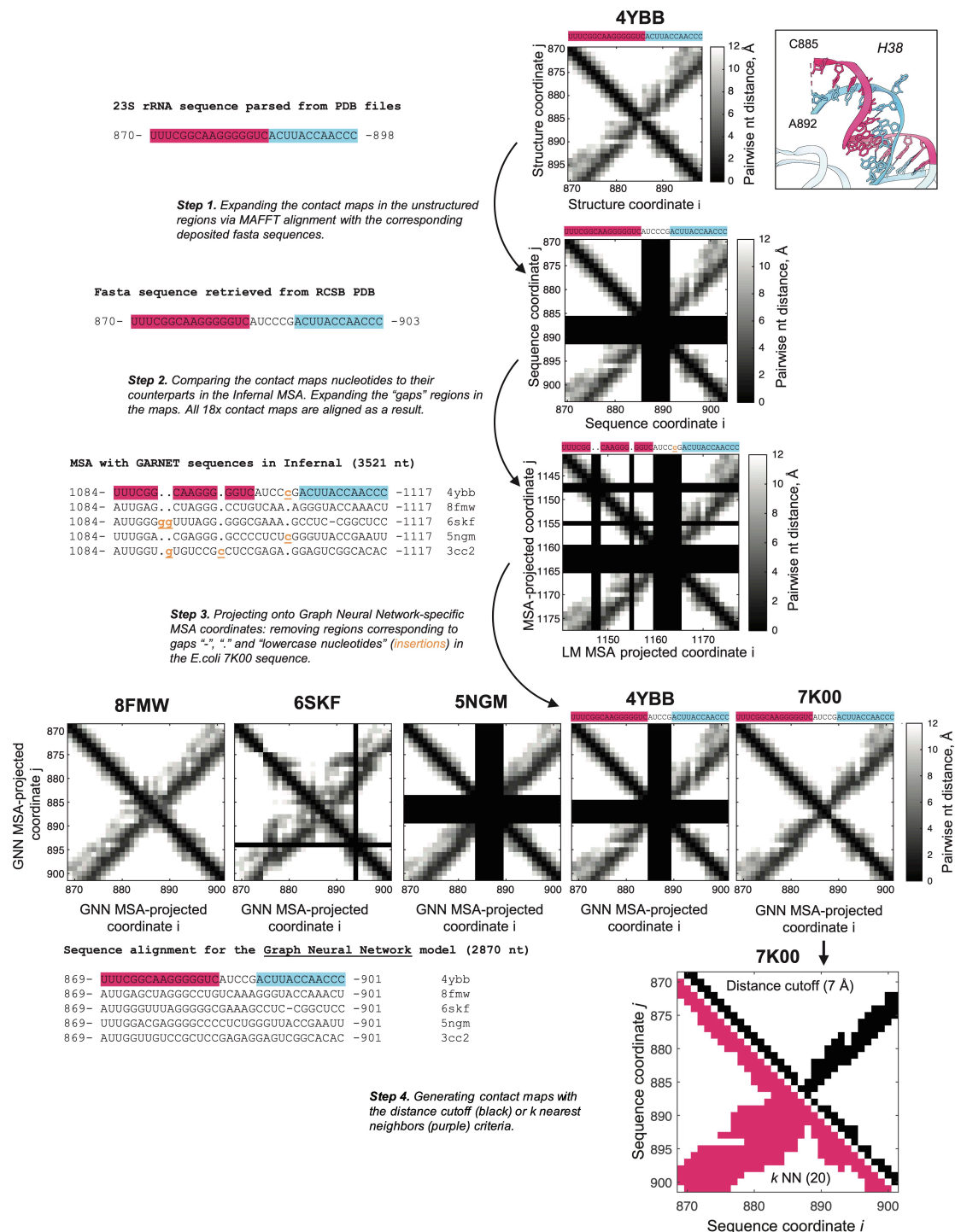


Supplementary Fig. 1: Additional evaluation of RNA dataset sequence diversity in GARNET. **a.** Number of GARNET sequences for rRNA and for the top twenty most abundant of the 228 RNA families. **b.** Total sequence length of GARNET RNA sequences for rRNA and for the top twenty most abundant of the 228 RNA families. **c.** Comparing diversity of GARNET-based alignments against state-of-the-art alignments for 23S rRNA, 16S rRNA, 5S rRNA by filtering the alignments at a range of pairwise fractional identity thresholds with esl-weight, part of the HMMER suite of programs⁵⁹. **d.** Diversity comparison for the three most abundant of the 228 RNA families in GARNET with esl-weight.



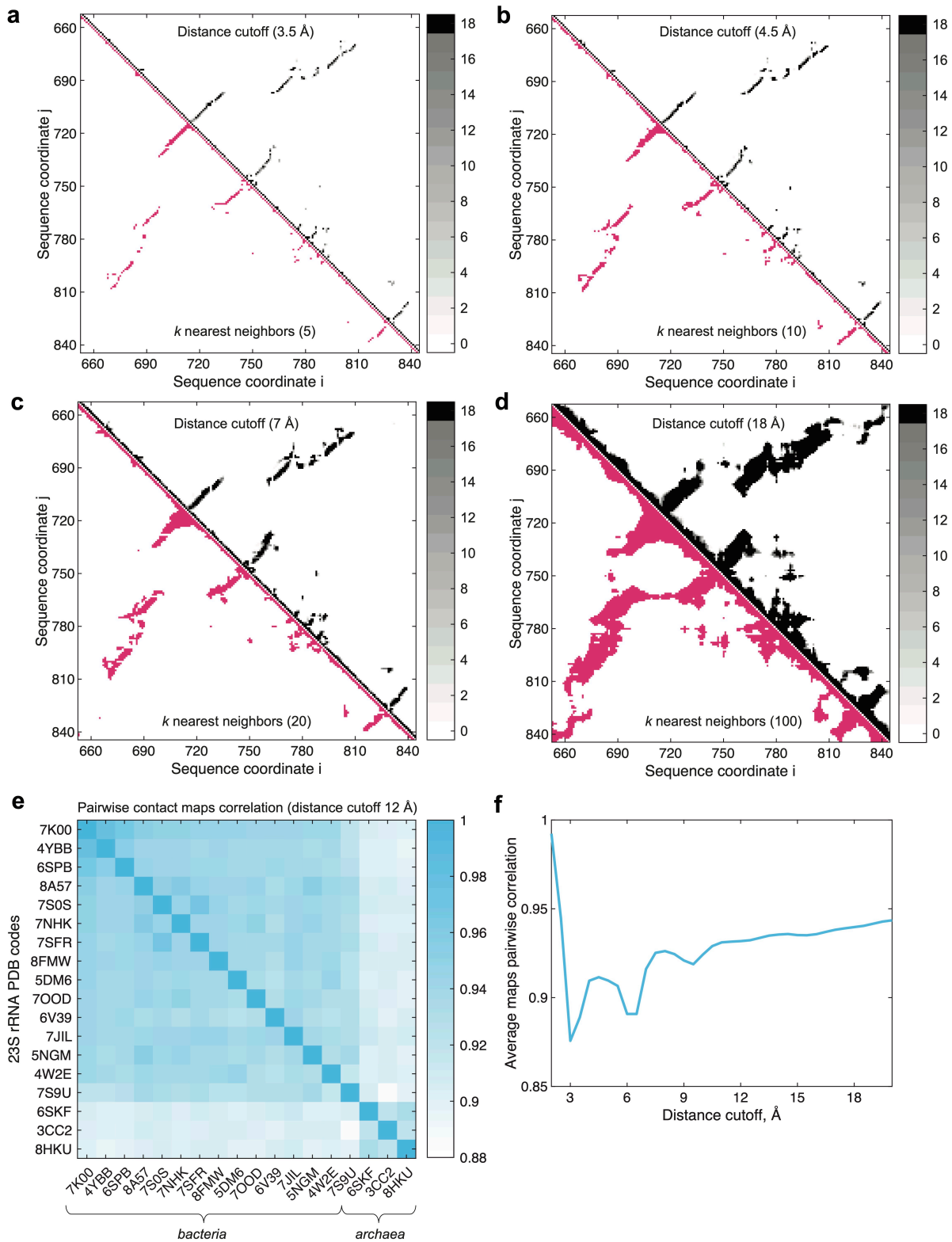
Supplementary Fig. 2: Bacterial phylogeny within the GTDB including OGTs.

Bacterial phylogenetic tree of GTDB reference organisms, grouped at the Class taxonomic rank, arbitrarily rooted. Node tip sizes are proportional to the number of species represented by node (\log_2 transformed). Inner circle indicates Phylum. The next circle represents TOME-predicted min, median, and maximal optimal growth temperatures of all species within rank. The next two circles similarly represent empirically measured optimal growth temperatures pulled from the Tempura and Gosha datasets, respectively. Outer circles represent the total number of 23S, 16S, and 5S detected in each rank, respectively (\log_2 transformed).



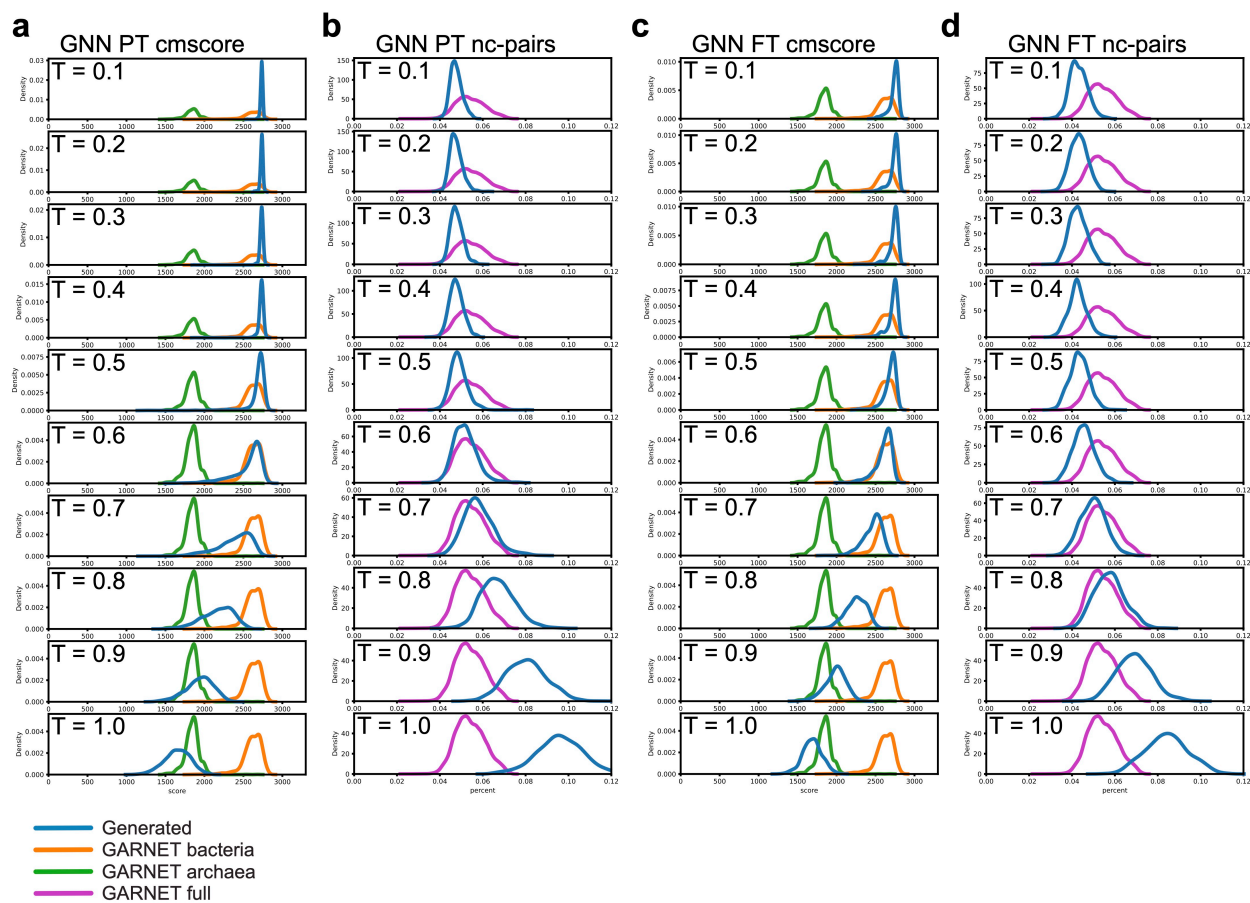
Supplementary Fig. 3: Schematic of MSA-informed alignment of distance matrices from ribosomal structures and generation of contact maps. The initial unaligned pairwise nucleotide distance matrices were generated from 23S rRNA structures in the

PDB files (see Methods). Further, sequences of 23S rRNA were extracted directly from the PDB files and corresponding FASTA files available in the Protein Data Bank³⁸. In the initial step, nucleotides missing in the structures were pinpointed through a MAFFT alignment comparing FASTA and PDB-derived sequences, leading to the insertion of empty columns and rows at these positions in the distance matrices. Subsequently, in step 2, the extracted archaeal and bacterial rRNA sequences from the structures (shown) were combined with those from GARNET using Infernal, matching the distance matrices' coordinates with the MSA with further introduction of empty rows and columns. At step 3, insertions (lowercase characters in the MSA) and deletions (gaps) were identified in the *E.coli* 7K00 sequence in the MSA, and the corresponding rows and columns were removed from the distance matrices. This process aligned the nucleotides in the distance matrices of all 18 archaeal and bacterial 23S rRNAs with their counterparts in the GARNET-anchored MSA utilized for the GNN model. In the final step, contact maps were generated from the distance matrices based either on the distance cutoff or *k*-nearest neighbors criteria (see Methods).

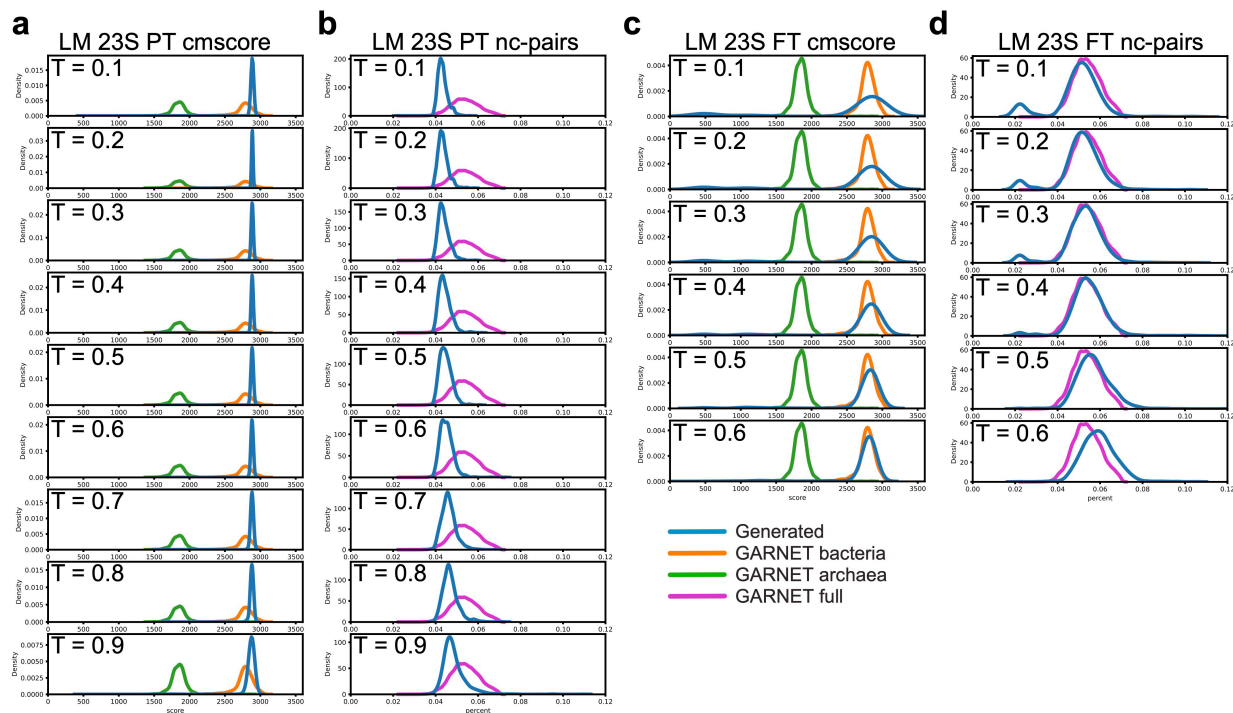


Supplementary Fig. 4: Contact maps and comparisons of high-resolution bacterial and archaeal 50S subunit structures. a-d. Comparison of contact maps generated for

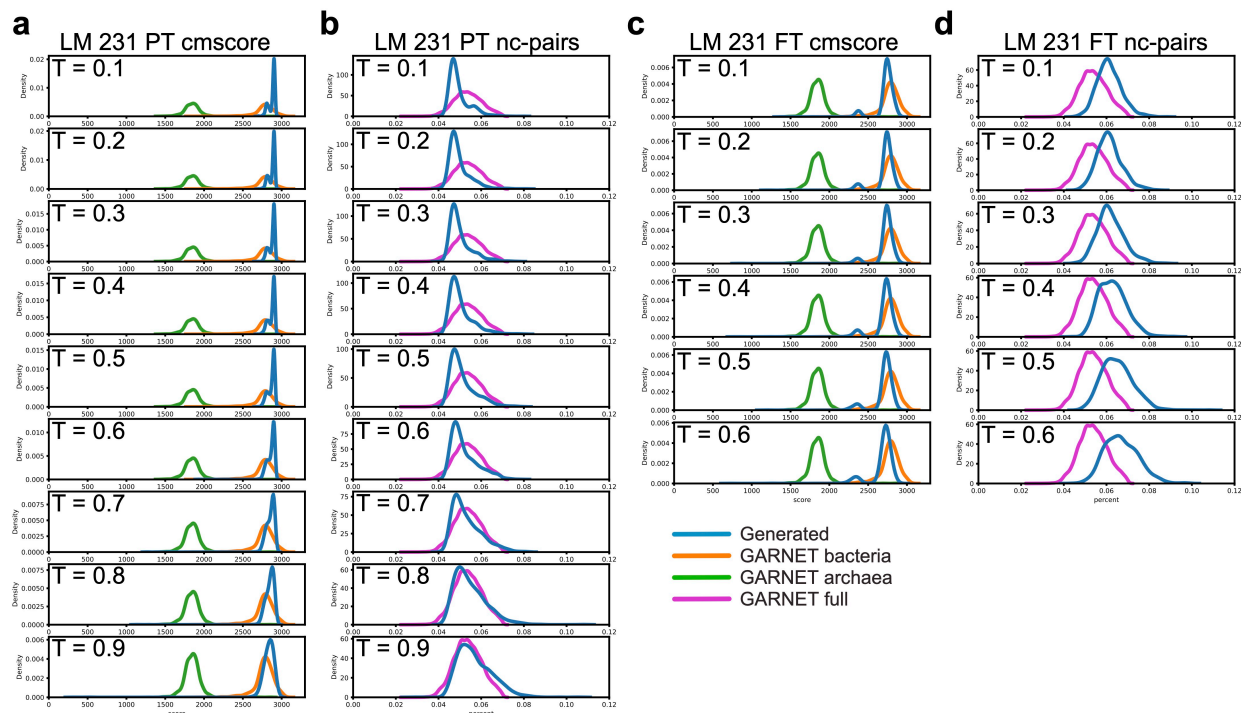
23S rRNA with the distance cutoff (top-right) and the k -nearest neighbors criteria (bottom-left). The matching pairs of fully sampled distances and k values for nearest neighbors were chosen according to the histogram in Fig. 3d. **e.** Pairwise correlation of contact maps for 18 bacterial and archaeal 23S rRNA structures, generated at a distance cutoff of 12 Å (see Methods). Note the high degree of structural correlation in the plot, which is also evident from matching of the 18 contact maps feature coordinates in panels (a) through (d). **f.** Average correlation of the 18 contact maps as a function of distance cutoff. Local maxima of correlation at 4.5 Å, 8 Å, 11 Å in the plot correspond to the minima between the peaks in Fig. 3d, indicating full sampling of 3.5 Å, 6 Å, 12 Å characteristic internucleotide distances. The structural correlation degree does not rise significantly above the distance cutoff of 12 Å.



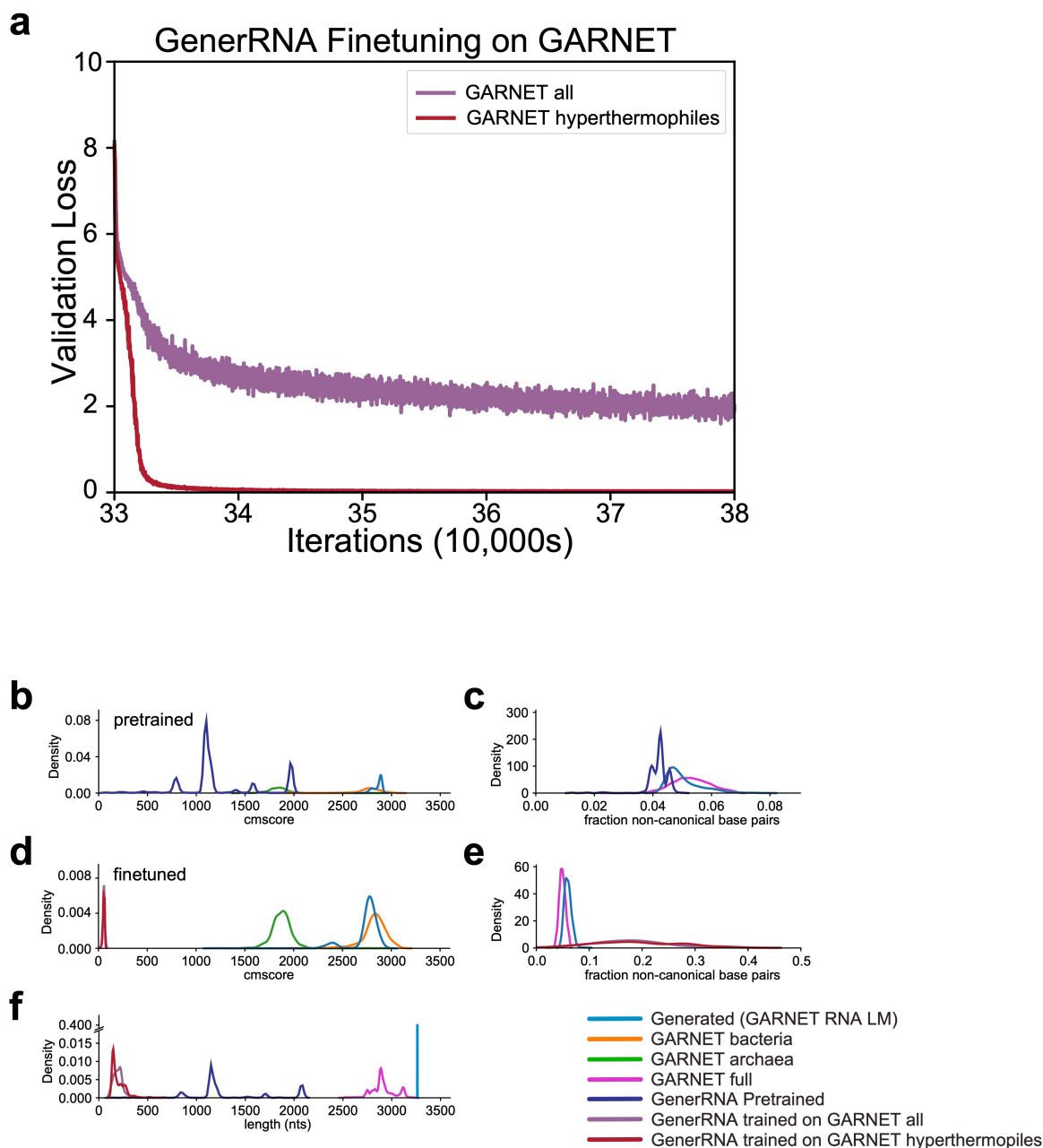
Supplementary Fig. 5: Properties of RNA sequences generated from the 23S rRNA GNN model. **a.** Cmsearch scores for sequences generated from the pretrained GNN model at temperatures ranging from 0.1 to 1.0. **b.** Fraction of mispaired nucleotides of sequences generated from the pretrained GNN model relative to RF02541 at temperatures ranging from 0.1 to 1.0. **c.** Cmsearch scores for sequences generated from the finetuned GNN model at temperatures ranging from 0.1 to 1.0. **d.** Fraction of mispaired nucleotides of sequences generated from the finetuned GNN model relative to RF02541 at temperatures ranging from 0.1 to 1.0.



Supplementary Fig. 6: Properties of RNA sequences generated from the 23S rRNA LM. **a.** CM scores for sequences generated from the pretrained 23S rRNA LM at temperatures ranging from 0.1 to 0.9. **b.** Fraction of mispaired nucleotides of sequences generated from the pretrained 23S rRNA LM relative to RF02541 at temperatures ranging from 0.1 to 0.9. **c.** CM scores for sequences generated from the finetuned 23S rRNA LM at temperatures ranging from 0.1 to 0.6. **d.** Fraction of mispaired nucleotides of sequences generated from the finetuned 23S rRNA LM relative to RF02541 at temperatures ranging from 0.1 to 0.6.

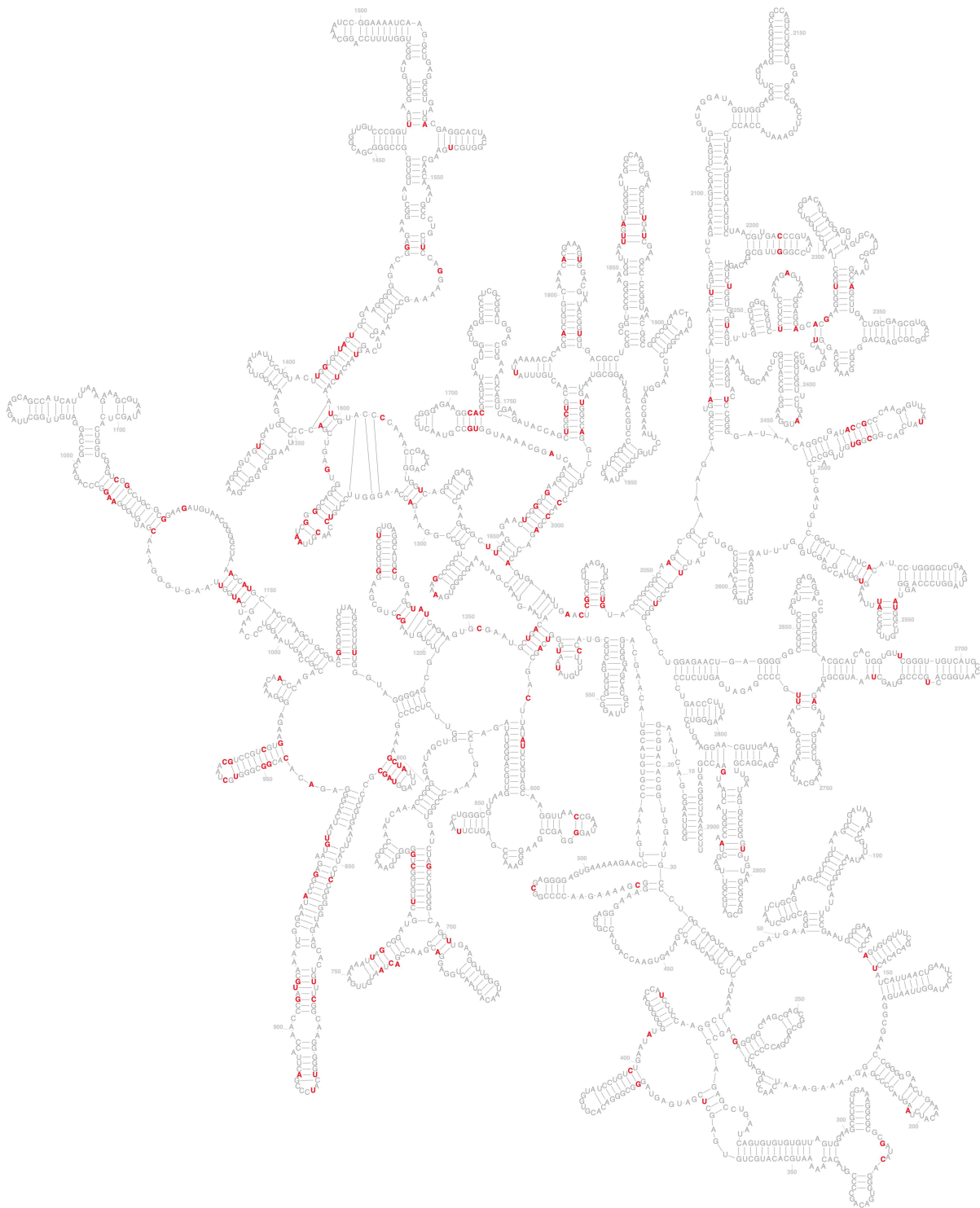


Supplementary Fig. 7: Properties of RNA sequences generated from the 23S rRNA LM models trained on the 231-RNA dataset. **a.** CM scores for sequences generated from the pretrained RNA LM model at temperatures ranging from 0.1 to 0.9. **b.** Fraction of mispaired nucleotides of sequences generated from the pretrained RNA LM relative to RF02541 at temperatures ranging from 0.1 to 0.9. **c.** CM scores for sequences generated from the finetuned RNA LM model at temperatures ranging from 0.1 to 0.6. **d.** Fraction of mispaired nucleotides of sequences generated from the finetuned RNA LM model relative to RF02541 at temperatures ranging from 0.1 to 0.6.

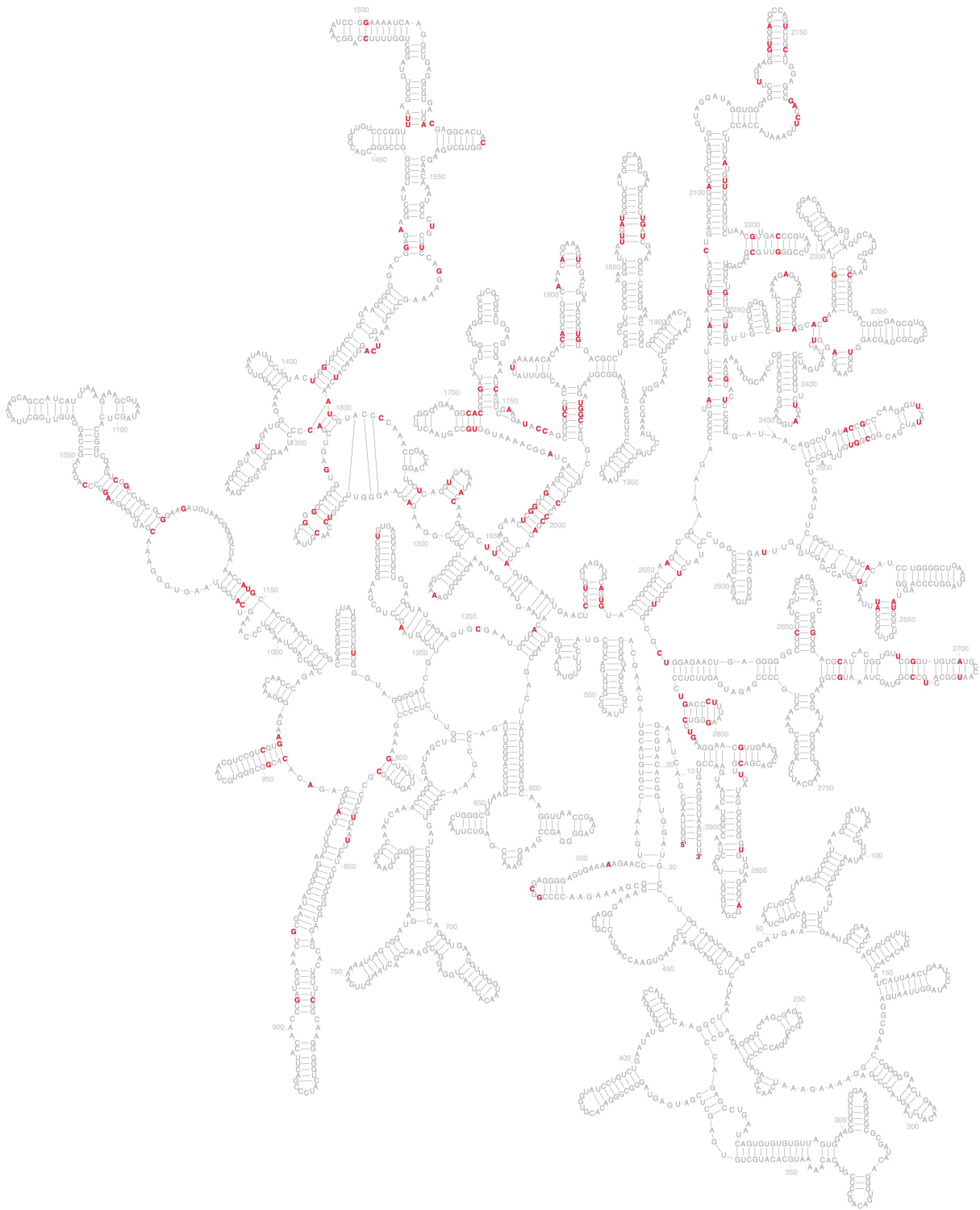


Supplementary Figure 8: GenerRNA finetuning and benchmarking. a. Validation loss values for the GenerRNA pretrained model finetuned on either GARNET-all or GARNET-hyperthermophile sequences. Validation sets were made using the default GenerRNA code. **b-c.** Cmsearch scores (**b**) and fraction of disrupted canonical base pairs (**c**) for sequences generated from the pretrained GenerRNA model. In (**b**) the cmsearch scores for GARNET natural and generated sequences are shown for reference. In (**c**) the fraction of disrupted canonical base pairs (i.e. Watson-Crick-

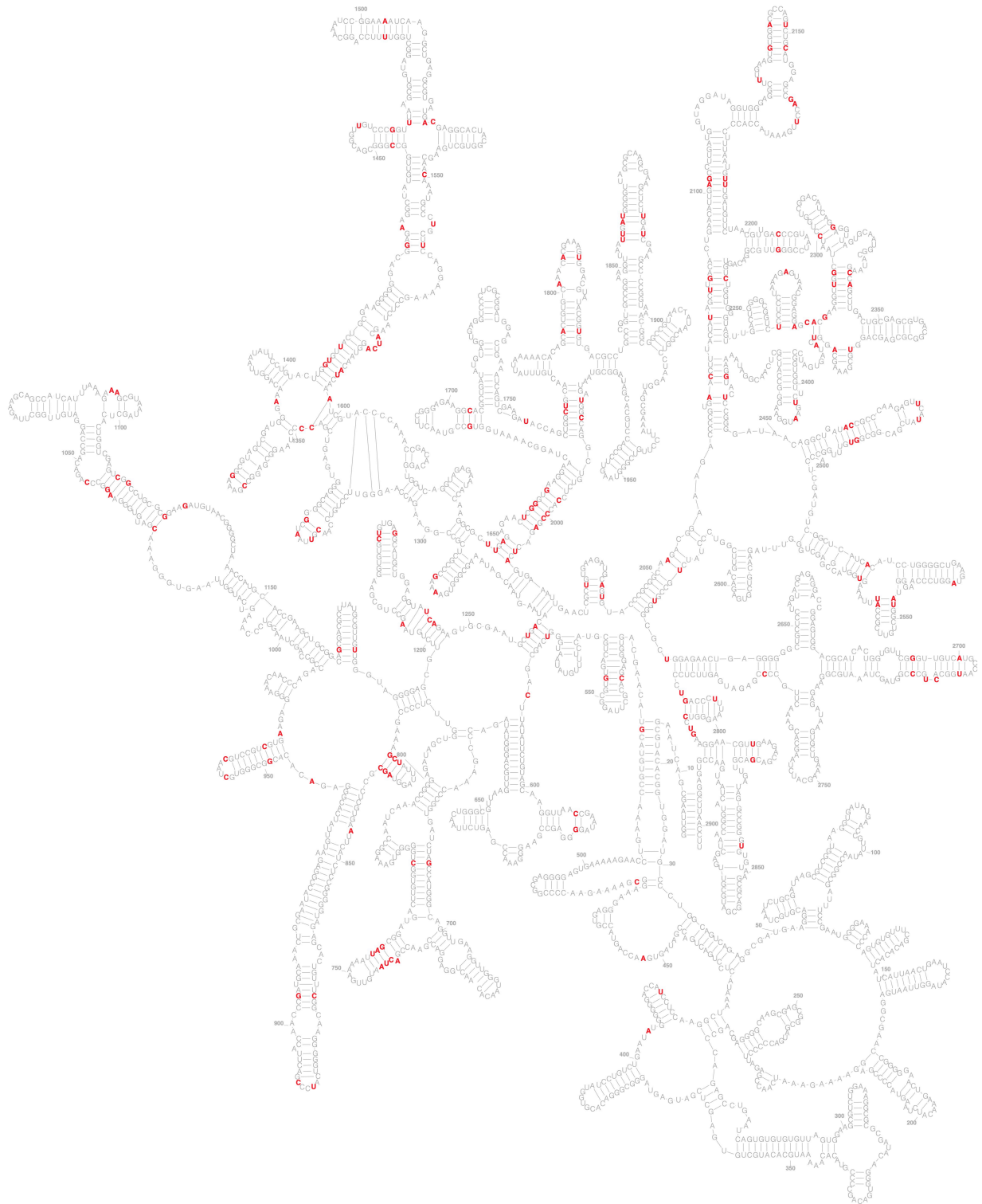
Franklin and G-U) relative to the Rfam RF02541 consensus secondary structure (denoted non-canonical base pairs) in the GenerRNA generated sequences are compared to naturally-occurring 23S rRNAs, and to sequences generated from the GARNET-all RNA LM. **d-e.** Cmsearch scores (**d**) and fraction of disrupted canonical base pairs (**e**) for sequences generated from the GenerRNA model finetuned on GARNET-all or GARNET-hyperthermophile sequences. **f.** Length of generated sequences from GenerRNA and GARNET RNA LM, compared to the natural distribution of sequence lengths in the GARNET database.



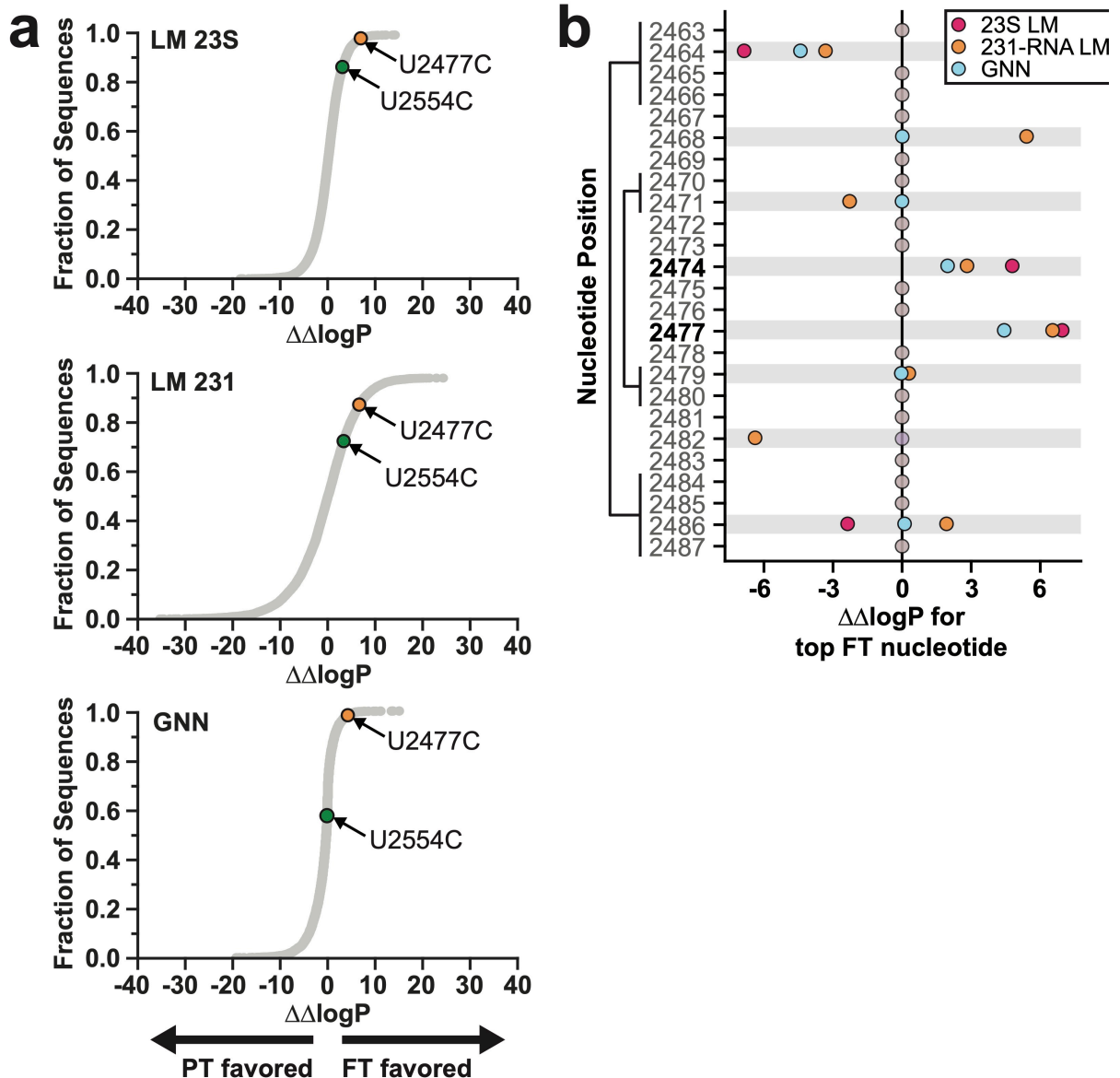
Supplementary Fig. 9: Top 200 JSD locations from the GNN model. Top ranking 200 Jensen-Shannon divergence values calculated from a secondary structure alignment of generated *E. coli* 23S rRNA sequences are colored in red.



Supplementary Fig. 10: Top 200 JSD locations from the 23S LM model. Top ranking 200 Jensen-Shannon divergence values calculated from a secondary structure alignment of generated *E. coli* 23S rRNA sequences are colored in red.

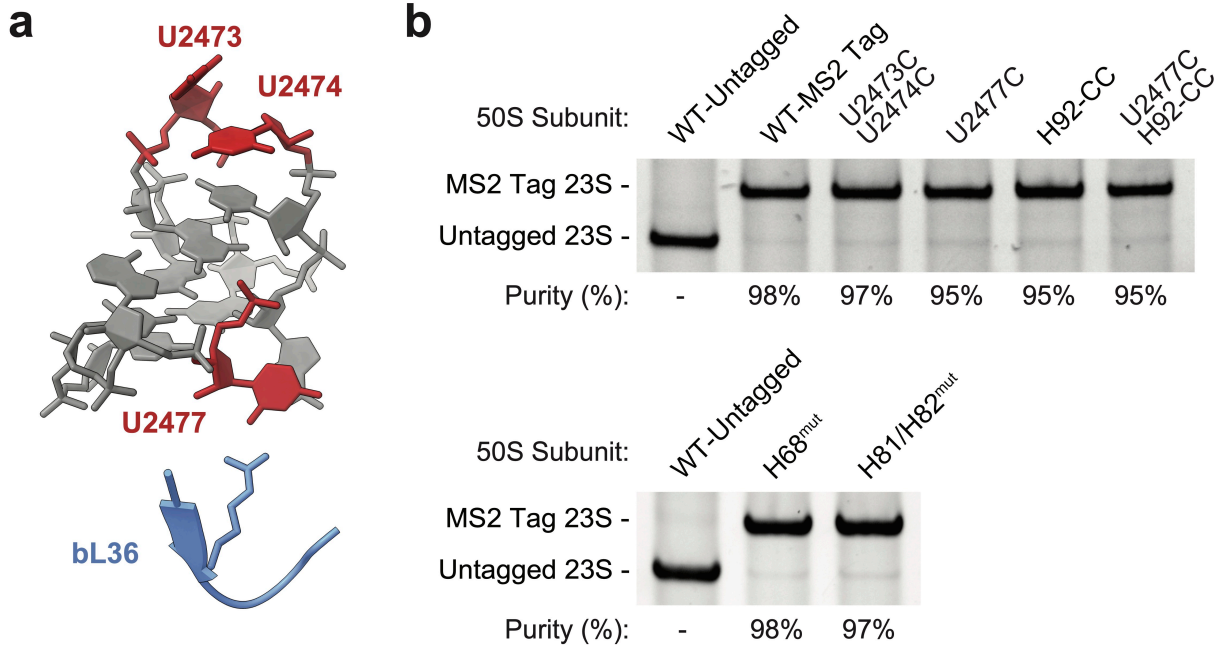


Supplementary Fig. 11: Top 200 JSD locations from the 231 RNA LM model. Top ranking 200 Jensen-Shannon divergence values calculated from a secondary structure alignment of generated *E. coli* 23S rRNA sequences are colored in red.



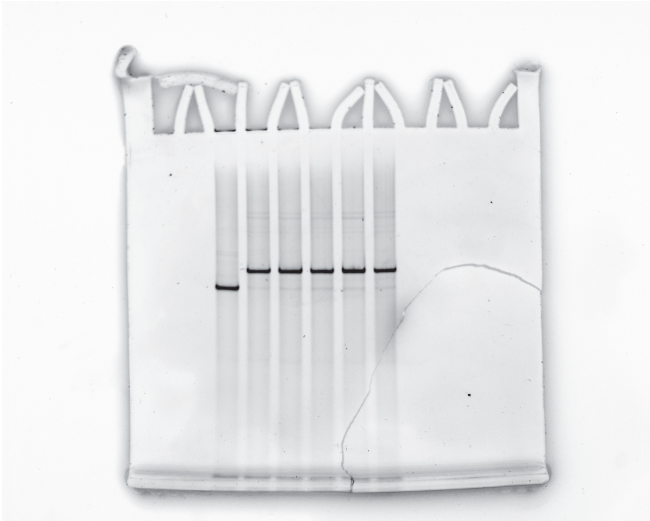
Supplementary Fig. 12: Analysis of $\Delta\Delta\log P$ values for mutations in helix H89. a. Cumulative plots of $\Delta\Delta\log P$ of all single mutations to the *E. coli* 23S rRNA for each model. Each point represents the probability of generating a single nucleotide mutant *E. coli* 23S sequence from the FT model relative to the PT model, normalized to that of the WT sequence. Two mutations, U2477C and U2554C, are denoted in orange and green, respectively. **b.** Analysis of helix 89 for candidate thermostabilizing mutations. For each position, the most frequent nucleotide in FT generated sequences (top FT nucleotide) is grafted into the *E. coli* 23S rRNA sequence and used to calculate $\Delta\Delta\log P(\text{FT-PT})$ for the 23S LM, 231-RNA LM, and GNN models. Positions where the top FT nucleotide differs

from WT in at least one model are highlighted in gray. Base pairing positions are indicated on the left.



Supplementary Fig. 13: Location and purification of rRNA mutations in the *E. coli* ribosome. **a.** H89 and bL36 in the *E. coli* ribosome (PDB:7K00). 23S rRNA positions that are mutated in this study are shown in red. **b.** After 50S purification, 23S rRNA was isolated and subjected to RT-PCR analysis to quantify endogenous WT 50S contamination. The band intensities of RT-PCR products were used to quantify sample purity. PCR products for untagged WT 23S (WT-untagged) are 114 base pairs, and for MST-tagged subunits (i.e. WT-MS2 Tag) are 147 base pairs.

Top gel:



Bottom gel:

